Achieving a Rapid Na+ Migration and Highly Reversible Phase Transition of NASICON for Sodium-Ion Batteries with Suppressed Voltage Hysteresis and Ultralong Lifespan

Qiao Wu, Yuanzhen Ma, Shengqiang Zhang, Xin Chen, Jinbo Bai, Hui Wang, Xiaojie Liu

Achieving a Rapid Na^+ Migration and Highly Reversible Phase Transition of NASICON for Sodium-Ion Batteries with Suppressed Voltage Hysteresis and Ultralong Lifespan

Qiao Wu[a], Yuanzhen Ma[a], Shengqiang Zhang[a], Xin Chen[a], Jinbo Bai[b], Hui Wang[a] and Xiaojie Liu[a,]*

[a] Key Laboratory of Synthetic and Natural Functional Molecule of the Ministry of Education, College of Chemistry & Materials Science, Northwest University, Xi'an 710127, P. R. China

[b] Laboratoire Mécanique des Sols, Structures et Matériaux (MSSMat), CNRS UMR 8579, Ecole CentraleSupélec, Université Paris-Saclay, 8-10 rue Joliot-Curie, 91190 Gif-sur-Yvette, France

Corresponding Author:

xiaojie.liu@nwu.edu.cn (X.Liu)

ABSTRACT

Sodium ion batteries have attracted great attention for large scale energy storage devices to replace lithium ion batteries. As a promising polyanionic cathode material of sodium-ion batteries, $Na_3V_2(PO_4)_2F_3$ (NVPF) belonging to NASICON exhibits large gap space and excellent structural stability, leading to a high energy density and ultralong cycle lifespan. To improve its stability and Na ion mobility, K^+ cations were introduced into NVPF crystal as in situ partial substitution for Na^+. The influence of K^+ in situ substitution on crystal structure, electronic properties, kinetic properties and electrochemical performance of NVPF were investigated. Through ex-situ examination, it turned out that K^+ occupied Na1 ion, in which the K^+ did not participate in the charge-discharge process and played a pillar role in improving the mobility of Na^+. Moreover, the doping of K^+ cation can reduce the band gap energy and improve the electronic conductivity. Besides, the optimal K^+ doping concentration in $N_{0.92}K_{0.08}$VPF/C was found so as to achieve rapid Na^+ migration and reversible phase transition. The specific capacity of $N_{0.92}K_{0.08}$VPF/C was as high as 128.8 mAh g^{-1} at 0.2 C, and at 10 C its rate performance was excellent, which showed a capacity of 113.3 mAh g^{-1}.

Keywords: $Na_3V_2(PO_4)_2F_3$; K^+ doping; Cathode material; Suppressed voltage hysteresis; Sodium ion batteries.

1. Introduction

Recently sodium-ion batteries (SIBs) have attracted great attention and been considered to substitute the dominant lithium-ion batteries (LIBs) in large scale energy storage devices (ESDs), because it not only has similar working principle to lithium-ion battery, but also has the superior advantages of abundant natural reserves, wide distribution and low cost of sodium resource [1-3]. In practical application, cathode materials with relatively low sodium storage capacity and insufficient electron/ion conductivity actually hinder the advancement of SIBs. Among the cathode materials of SIBs, compounds with Na superionic conductor (NASCION type) structure have become one of the most promising candidates because their three-dimensional open frame can generate a large number of gaps and enable rapid insertion and extraction of Na^+ with small lattice strains [4-5]. Owing to its high energy density, large gap space and excellent structural stability, $Na_3V_2(PO_4)_2F_3$ (NVPF) as a polyanionic compound with NASCION type structure has been extensively investigated. The crystal structure of NVPF is composed of $[VO_4F_2]$ octahedron and $[PO_4]$ tetrahedral units. Adjacent octahedrons are connected by F atoms, and $[PO_4]$ units are connected by O atoms, which form an extended three-dimensional framework with large tunnels along [110] and [1-10] directions, which is beneficial to Na^+ migration [6-9]. While, due to the insulation of $[PO_4]$ unit and the large deformation of NVPF, the electronic conductivity of NVPF is very low (2.4×10^{-12} S cm^{-1}), particularly together with the sluggish sodium ion diffusion via NVPF crystal, eventually causing low capacity and poor rate capability. In addition, NVPF has three pairs of redox potentials (~3.4, ~3.7 and ~4.2 V), but in the discharge process, owing to the polarization and structural variation, a large voltage hysteresis of NVPF occurs, giving rise to substantial energy loss, poor reversibility and short cycling lifespan. The main reason of hysteresis lies in the structural change and insufficient Na^+ migration of NVPF caused by the Na^+ insertion/desertion. Specifically, the dissipative hysteresis can be ascribed to the slow diffusion and poor surface mobilities of Na^+, leading to large concentration gradients and overpotentials in electrode particles. On the other

hand, a non-dissipative hysteresis can be attributed to kinetic dissipation and mostly to a qualitative path change in the discharge reaction compared to the charge reaction. Therefore, to address the issue of NVPF with large voltage hysteresis and short cycling lifespan, finding an effective pathway to improve the structural stability and Na^+ diffusion of NVPF has been a crucial task.

Until now, heteroatom doping has been widely explored and considered as a useful strategy to deal with the voltage hysteresis and cycle lifespan issues. As is well known, the building of heteroatom doping can bring in the expanded crystal cell and especially the enlarged interlamellar spacing or octahedral/tetrahedral centers, and modulate the intrinsic physiochemical property of crystal, which enable the sodium ions transport easily and efficiently without devastating structural collapse, consequently resulting in the diminished voltage hysteresis and superior cycling during charge/discharge. Particularly, the cation doping has drawn great attention and has been commonly used in modifying cathode materials for SIBs because the cations can reduce the bandgap and elevate the density of state near the fermi level remarkedly. Likewise, the doping cations can work as functional pillar ions to broaden the sodium ion diffusion channels and mitigate the structural distortion and internal stress of the regulated cathode materials with highly reversible phase transition during repeated cycling. As for NVPF, in the literature the most widely studied method has been the doping of transition metals occupied in V position of NVPF crystal cell, where the $[V_2O_8F_3]$ dioctahedral unit can be adjusted by the doped cations, to boost the Na^+ migration and electron transfer in NVPF crystalline structure. So far, various cations such as Y^{3+}[10], Mg^{2+} [11], Cr^{3+} [12], Mn^{2+} [13] and Ti^{4+} [14] have been applied as dopants for NVPF-based materials to improve ion/electron conductivity and reinforce the structural stability, exhibiting the ameliorated electrochemical performance. For instance, Liu et al. introduced Y^{3+} into the V position of NVPF/C using sol-gel method. They found that by doping Y^{3+} with a larger radius, a larger lattice distance was created, which is conducive to Na^+ migration. Meanwhile, thanks to the weaker Y-O bond than the V-O bond, it was displayed that the intrinsic electron conductivity of Y-doped NVPF was increased to a degree. Moreover, as Y^{3+} does not participate in

electrochemical process, the Y cation can play a pillar role in alleviating the crystal deformation of NVPF and improving the structural stability of NVPF during charge/discharge.[10] Notwithstanding, compared with the above pathway of the doped cations in V position of NVPF, the mechanism of cation substituted Na^+ sites in dealing with the voltage hysteresis of SIBs has been unclear and less investigated by researchers. Inspired by the advantages of cation doping in NVPF, it is assumed that K^+ might be utilized as doped cation to replace Na^+ via in situ substitution in the lattice of NVPF and expand the diffusion channels of Na^+, since K^+ and Na^+ belong to the same main family (alkaline metals) and have similar chemical properties. Moreover, the radius of K^+ (~138 pm) is larger than that of Na^+ (~102 pm), which can result in the enlarged Na^+ diffusion pathway with subtle change in crystal structure and a highly reversible phase transition of NVPF during sodiation and (de) sodiation process. Beyond that, K^+ is less electronegative than Na^+, which improves the electronic conductivity. Note that there is usually an optimal concentration of doped cations in the NVPF modification. As is well known, the larger amount of doping cations, the more enlarged crystal of doped NVPF, favoring the rapid Na^+ migration[15]. Whereas, when the doping amount is increased continuously over the optimal concentration of doped cations, the structural stability of doped NVPF will be sacrificed during sodiation and (de)sodiation, leading to a poor reversibility. Therefore, achieving rapid Na^+ diffusion and reversible phase transition is great of importance and urgence by finding the optimal doping concentration for high performance sodium-ion batteries. Unfortunately, the mechanism of K^+ doping for replacing Na^+ in NVPF via a partial in situ substitution has not studied by researchers. In addition, how much the optimal doping concentration of K^+ in NVPF needs to be found.

Hence, in our work, we have successfully synthesized an array of K-doped $Na_3V_2(PO_4)_2F_3$ materials with varied K contents via in situ substitution, in combination with a uniform carbon layer coating (named as $N_{1-x}K_xVPF/C$ (x=0, 0.03, 0.08, and 0.13)), by sol-gel method (Figure 1a). Regarding the voltage hysteresis and cycle lifespan, the advantageous features of $N_{1-x}K_xVPF/C$ composite can be summarized as follows (Figure 1b): 1) K^+ cation doping can improve the inherent

electronic conductivity of NVPF by reducing the band gap energy without affecting the valence state of V; 2) The appropriate K^+ cation doping can enlarge the migration channels of Na^+ ascribed to the larger radius of K^+ and give rise to a highly reversible phase transition of K-doped NVPF. 3) The K^+ cation doping occurs at the Na1 position, where the doped K+ does not participate in the overall embedding/releasing process in electrochemistry. Instead, it solely acts as a stabilizing pillar to improve the material's stability. When tested as the cathode material for sodium ion batteries, the as-obtained $N_{0.92}K_{0.08}$VPF/C sample manifested the highest conductivity and structural stability, thus delivering the most remarkable electrochemical performance. In detail, the specific capacity of $N_{0.92}K_{0.08}$VPF/C was as high as 128.8 mAh g^{-1} at 0.2 C, and at 10 C its rate performance was excellent, which showed a capacity of 113.3 mAh g^{-1}. At a low rate of 0.2 C, a high retention of 92% was obtained after 100 cycles, and meanwhile after ultralong lifespan of 5000 cycles at a rate of 10 C, the retention rate was as high as 60.2%.

2. Results and Discussion

The schematic diagram of K^+ substituted three-dimensional NASICON framework of NVPF was illustrated in Figure 1a. The crystal structure of NVPF is in the space group $P4_2/mnm$, belonging to an orthorhombic crystal system [16]. Figure 1b revealed the schematic illustration of NVPF crystal structure, where Na1 position is occupied by K^+ cation in situ, giving rise to the reduction of band gap energy and fast Na^+ diffusion through $N_{1-x}K_x$VPF. Moreover, Figure 1c displayed a scheme presenting the Na^+ diffusion in $N_{0.92}K_{0.08}$VPF structure and Na^+ migration energy by DFT calculation.

To examine the crystal structure, XRD patterns of $N_{1-x}K_x$VPF/C (x = 0, 0.03, 0.08, and 0.13) samples were recorded, as shown in Figure 2a. As can be seen, all the diffraction peaks of $N_{1-x}K_x$VPF/C corresponded to the space group of $P4_2/mnm$ (ICDD PDF No.01-089-8488)[17-18], demonstrating that small amount of K^+ cation doping displayed no change in the crystal structure and no reflected peaks of impurities appeared. Moreover, a partial view of XRD patterns was enlarged in the

degree range of 25 to 35° (in Figure 2b). It was observed that with the increase of K^+ content, the diffraction peaks representing (220), (113) and (222) crystal planes were shifted to a small angle, leading to the conclusion that the more substitution of K^+, the more expanded the NKVPF crystal, which is conducive to the migration of Na^+.

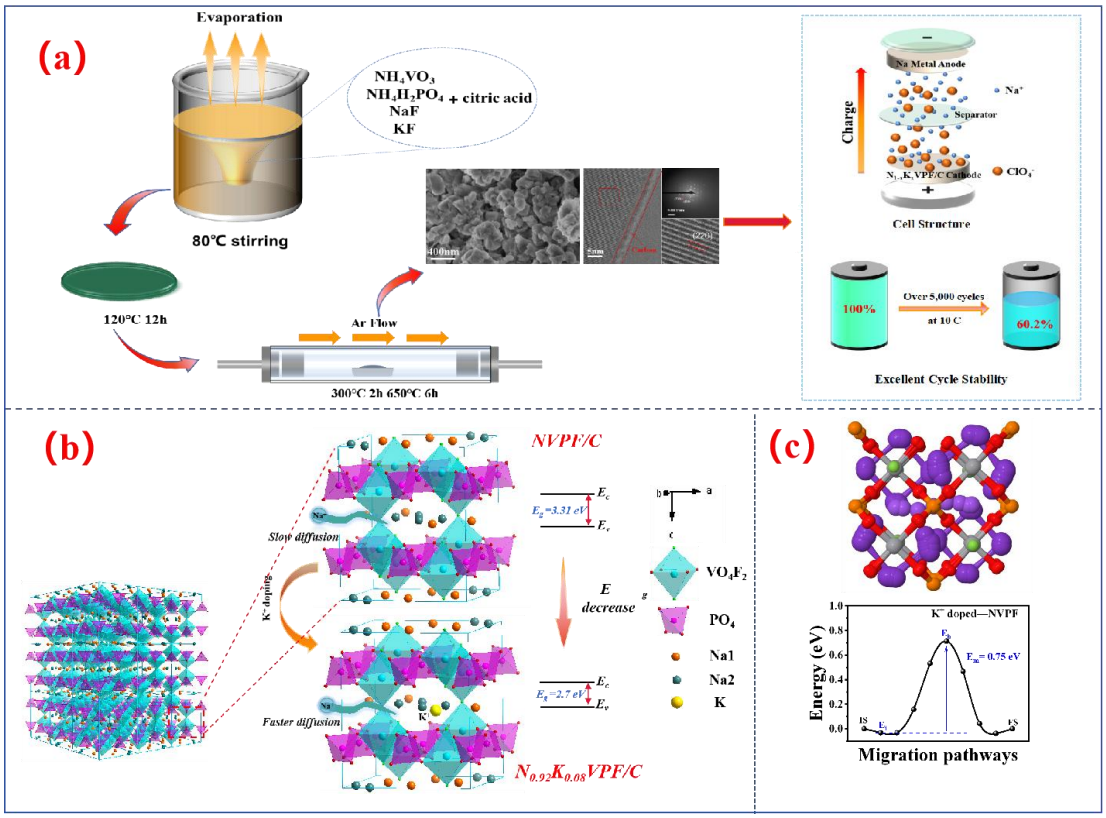

Figure 1 (a) Schematic illustrations for the synthesis process of $N_{1-x}K_xVPF/C$ (x=0, 0.03, 0.08 and 0.13) samples by sol-gel method and for the cell configuration of SIBs and excellent cycle stability. (b) Scheme presenting the NVPF crystal structure, where Na1 position is occupied by K^+ cation, giving rise to the reduction of band gap energy and faster Na^+ diffusion through $N_{0.92}K_{0.08}VPF$. (c) Scheme presenting the Na^+ diffusion in $N_{0.92}K_{0.08}VPF$ structure and Na^+ migration energy by DFT.

In order to determine the doping content of K^+ cation in NVPF, inductively coupled plasma mass spectrometry (ICP-MS) was employed. As indicated in Table S1, the K^+ content of the doped NVPF could be calculated as 0%, 3.06%, 7.96% and 12.98% respectively, by taking the V content as the constant value. Correspondingly, x in $N_{1-x}K_xVPF/C$ samples was 0, 0.03, 0.08, and 0.13, respectively, and was approximately equal to the amount of added K^+ cations, and the deviation is small. SEM and TEM were also used to observe the morphologies and microstructures of

$N_{1-x}K_xVPF/C$ (x = 0, 0.03, 0.08 and 0.13) with different amounts of K^+. Figure 2c-d and Figure S1 displayed that all the samples had irregular particle sizes and shapes and some agglomeration.

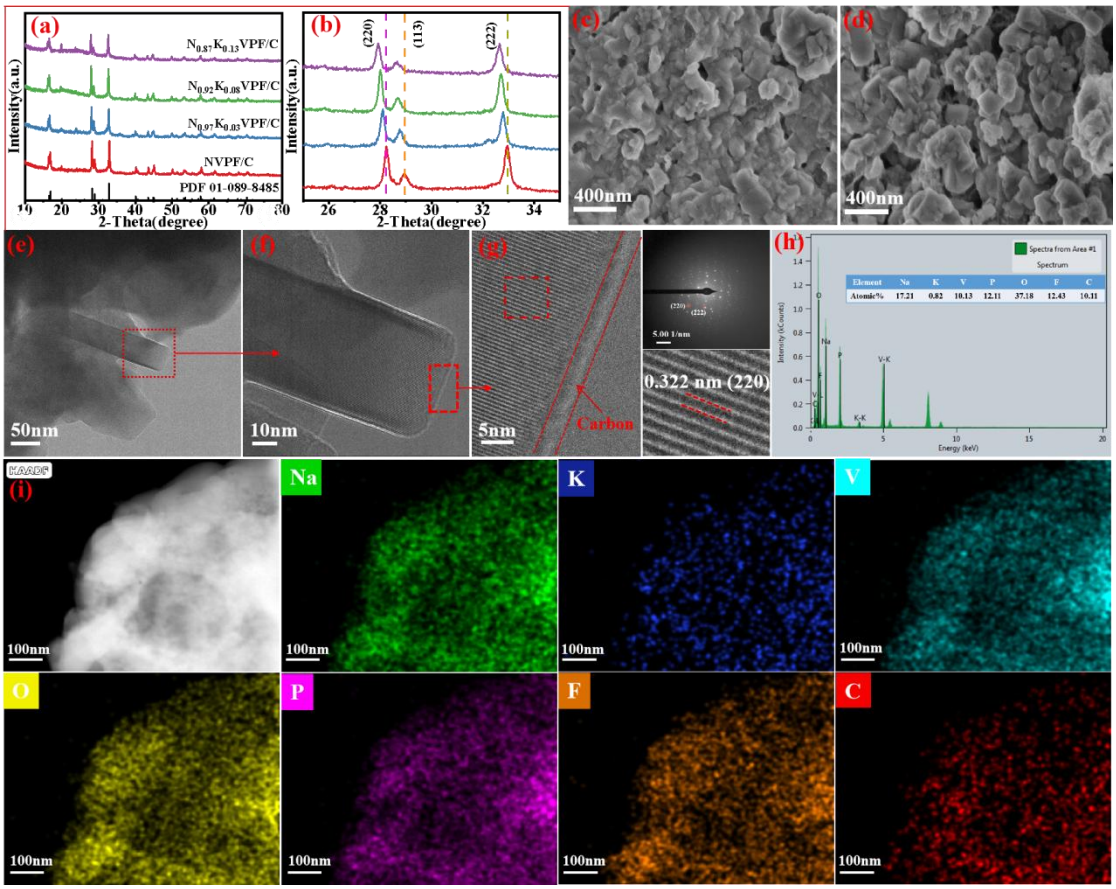

Figure 2. (a) XRD patterns of $N_{1-x}K_xVPF/C$ samples; (b) a partial enlarged view of XRD patterns in the degree range of 25 to 35°. SEM images of (c) NVPF/C and (d) $N_{0.92}K_{0.08}VPF/C$. (e-f) TEM images of $N_{0.92}K_{0.08}VPF/C$ with different magnification. (g) HRTEM images and SAED of $N_{0.92}K_{0.08}VPF/C$. (h) EDS spectrum of $N_{0.92}K_{0.08}VPF/C$ and (i) The corresponding elemental mappings of Na, K, V, P, O, C and F.

With the increase of K^+ content, the particle size of $N_{1-x}K_xVPF/C$ decreased gradually, showing that the doping of K^+ can effectively reduce the agglomeration in the process of material synthesis [19]. From TEM images of $N_{0.92}K_{0.08}VPF/C$ in Figure 2e-f, it can be observed that the sample had the characteristics of irregular layer-like morphology. Figure 2g represented the HRTEM images of $N_{0.92}K_{0.08}VPF/C$, manifesting a highly crystalline structure with lattice distance of 0.322 nm in accordance with the (220) plane of NVPF and a uniform carbon coating layer with 4 nm on the NVPF surface

[20-21]. Meanwhile, the selected area electron diffraction (SAED, selected in the red square) of $N_{0.92}K_{0.08}$VPF/C with many obvious spots confirmed the single crystalline structure. The energy dispersive X-ray analysis (EDS) in Figure 2h showed that the atomic ratios of Na: K: V: P: F elements were close to the stoichiometric configuration of $Na_{0.92}K_{0.08}$VPF/C. Besides, Figure 2i exhibited the TEM elemental mapping images of all elements for the $Na_{0.92}K_{0.08}$VPF/C sample, displaying the homogenous elemental distribution of Na, K, V, C, P, O and F. As for NVPF/C, $N_{0.97}K_{0.03}$VPF/C and $N_{0.87}K_{0.13}$VPF/C samples, the low magnification TEM (Figure S2a, d and g) indicated the aggregation of nanoparticles for all the other samples, confirming with SEM observation. Higher magnification TEM (Figure S2b, c and h) exhibited that noticeable crystalline planes were seen and the amorphous carbon layers with approximately 4 nm were present on the surfaces of all the samples. In addition, the SAED mode (photographed in a single particle, Figure S2c, f, and i) revealed many distinct crystal-plane spots and lattice fringes, matching with TEM results and indicating a high crystallinity of the as-prepared samples. Fourier Transform infrared spectroscopy (FT-IR) of $N_{1-x}K_x$VPF/C between 400-2400 cm^{-1} were carried out to detect changes in functional groups.

In Figure 3a, the weak absorption band at ~1631 cm^{-1} was consistent with the O-H bending vibration of C-OH group. The wide band at 1000 ~ 1150 cm^{-1} could be attributed to the asymmetric stretching vibration (V_{as}) of the PO_4^{3-} tetrahedron. The vibration of V-F bond and the stretching vibration of the V-O bond were ascribed to ~948 cm^{-1} and 921cm^{-1}, respectively. The absorption at 675 cm^{-1} and 553 cm^{-1} were attributed to the symmetric stretching and bending vibration of the P-O bond, and asymmetric bending vibration v(F_2) of PO_4^{3-} at 556 cm^{-1} [22]. FT-IR showed that all the samples delivered similar functional groups and binding states of the amorphous carbon [23]. The content of carbon layer was evaluated by thermogravimetric analysis (TGA). As illustrated in Figure 3b, the $N_{1-x}K_x$VPF/C (x = 0, 0.03, 0.08 and 0.13) with different K^+ contents offered close carbon contents of ~2.8wt%, ~3.2wt%, ~2.7wt% and ~2.9wt%, respectively, meaning that K^+ cation doping had no influence on the carbon content [24]. The characteristic raman spectra

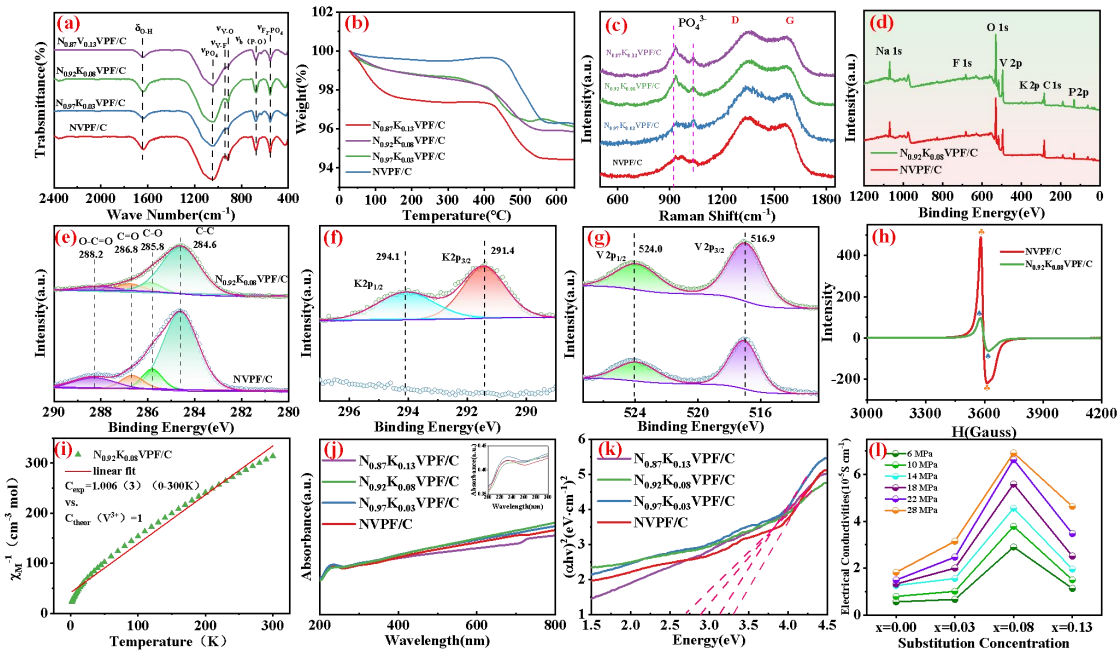

Figure 3 (a) FTIR spectra of $N_{1-x}K_xVPF/C$ (x=0, 0.03, 0.08, 0.13) samples. (b) TGA curves under air atmosphere of $N_{1-x}K_xVPF/C$ (x=0, 0.03, 0.08, 0.13) samples. (c) Raman spectra of $N_{1-x}K_xVPF/C$ (x=0,0.03,0.08,0.13) samples. (d) Full XPS spectra of NVPF/C and $N_{0.92}K_{0.08}VPF/C$. (e) C 1s XPS spectra of NVPF/C and $N_{0.92}K_{0.08}VPF/C$. (f) K 2p XPS spectra of NVPF/C and $N_{0.92}K_{0.08}VPF/C$. (g) V 2p XPS spectra of NVPF/C and $N_{0.92}K_{0.08}VPF/C$. (h) EPR spectra of NVPF/C and $N_{0.92}K_{0.08}VPF/C$. (i) SQUID measurement of $N_{0.92}K_{0.08}VPF/C$ between 0-300 K and a linear fitting. (j) Plots of UV-vis absorption and inset shows the 200-300nm absorption. (k) The corresponding band gaps of $N_{1-x}K_xVPF/C$ (x=0, 0.03, 0.08, 0.13) samples by the estimation of fitted absorption edges (magenta lines). (l) Electronic conductivities of $N_{1-x}K_xVPF/C$ (x=0, 0.03, 0.08, 0.13) samples.

of $N_{1-x}K_xVPF/C$ (x= 0, 0.03, 0.08, and 0.13) (in the range of 500-1875 cm^{-1}) were shown in Figure 3c. The bands at 942 and 1048 cm^{-1} were P-O symmetric stretching vibration and asymmetric stretching vibration inside PO_4^{3-}, respectively [25]. 1350 and 1581cm^{-1} bands were observed in all samples, attributed to disordered carbon (D band, sp^3 type) and graphite carbon (G band, sp^2 type), respectively [26-27]. The I_D/I_G ratio values for the $N_{1-x}K_xVPF/C$ (x =0, 0.03, 0.08, and 0.13) samples were 1.15,1.16,1.15 and 1.15, respectively, suggesting that the graphitization degree of carbon was almost the same in all samples. In short, NVPF materials with different K^+ content had the similar carbon coating, carbon content and carbon binding state. To further prove the

presence of K^+ cation and the electronic states of V metal, the as-prepared NVPF/C and $N_{0.92}K_{0.08}VPF/C$ composites were further measured by XPS (in Figure 3d-g). As showed in Figure 3d, the presence of K, Na, F, P, O, V and C elements were confirmed by the XPS spectrum in the full scan. The simulated XPS experimental value and fitted curve of C 1s in NVPF/C and $N_{0.92}K_{0.08}VPF/C$ can be deconvolved into four Gaussian peaks (Figure 3e), which represented C-C (284.6 eV), C-O (285.8 eV), C=O (286.8 eV) and O-C=O (288.2 eV), respectively [23, 28]. This observation signified that the C status was mainly C-C and that there was the existence of less oxidizing groups, which might be due to the decomposition of limonic acid in the synthesis process. Figure 3f indicated that in the case of $N_{0.92}K_{0.08}VPF/C$, the K $2p_{1/2}$ and K $2p_{3/2}$ peaks were located at 294.1 eV and 291.4 eV, respectively, while no K peaks were found in NVPF/C, which verified the successful doping of K^+ cations in $N_{0.92}K_{0.08}VPF/C$. As seen in Figure 3g, the binding energy of V can be clearly observed at 516.9 eV and 524.0 eV, which can be attributed by V $2p_{3/2}$ and V $3p_{1/2}$ of V^{3+} respectively, in consistence with the pure phase of $Na_3V_2(PO_4)_2F_3$ structure [29]. In Figure S3, compared with the F 1s peak of NVPF/C at 684.1 eV, that of $N_{0.92}K_{0.08}VPF/C$ sample was shifted to the higher binding energy of 684.3 eV, indicating that a small amount of K doping affected the local electron structure around F in NVPF/C [30-31]. The samples were also characterized by Electronic Paramagnetic Resonance (EPR). The EPR spectra of NVPF/C and $N_{0.92}K_{0.08}VPF/C$ samples were depicted in Figure 3h, illustrating an axial signal centered at 3598 Gauss with g=1.95 [32]. Clearly, it was seen that the NVPF/C and $N_{0.92}K_{0.08}VPF/C$ had the same crystalline structure. Moreover, the EPR spectra signal of NVPF/C and $N_{0.92}K_{0.08}VPF/C$ corresponded to V^{3+} with the unpaired electrons, clearly demonstrating that the valence state of V in the samples was V^{3+} and that the doping of K^+ had no change in the valence state of V. In addition, the intensity of $N_{0.92}K_{0.08}VPF/C$ is much weaker than that of NVPF/C, the result of which is due to the K^+ cation doping. To further confirm the vanadium oxidation state, magnetic susceptibility measurements were performed (Figure 3i). According to the Curie-Weiss law $1/\chi_M=(T-\theta)/C$, where χ_M, T, θ and C are the molar magnetic

susceptibility, the absolute temperature, the asymptotic Curie temperature, and the Curie constant, respectively, the Curie constant C=1.006 (3) could be obtained by linear fitting of the data in the 0-300 K region, in remarkable agreement with the previous conclusion about the approximate theoretical value of C=1 [8, 33]. And, the approximate theoretical value of n=2 was obtained by $\chi_T=((1/8)n(n+2))$, where n is the number of unpaired electrons about vanadium, corresponding to V^{3+}. The asymptotic Curie temperatures (θ) of $N_{0.92}K_{0.08}VPF/C$ sample was -41.5(2.5) K, larger than the theoretical value of θ = -69(7) K, which is because of the K^+ doping. By comparing the analysis of NVPF/C and $N_{0.92}K_{0.08}VPF/C$, it was confirmed that only V^{3+} was present in NKVPF, corresponding to the $Na_3V_2(PO_4)_2F_3$ phase.

UV-Vis diffuse reflectance spectra of $N_{1-x}K_xVPF/C$ (x=0, 0.03, 0.08 and 0.13) samples were shown in the Figure 3j. Regardless of the added amount of K cations, a weak absorption peak between 200 nm-300 nm were found. Owing to the NVPF as a direct bandgap semiconductor, the optical absorption near the band edge is assumed to follow the formula $\alpha h\upsilon = A(h\upsilon-E_g)^{n/2}$ (n=1), where a, υ, E_g and A are the absorption coefficient, light frequency, band gap, and a constant, respectively [34-35]. The band gap energy (E_g value) of $N_{1-x}K_xVPF$ /C (x=0, 0.03, 0.08 and 0.13) could be thus estimated from a plot $(\alpha h\upsilon)^2$ versus photon energy (hυ). Correspondingly, the tangent lines of the graphs hυ and $(\alpha h\upsilon)^2$ were plotted in Figure 3k, and the intersection of the tangent line with the X-axis was the estimated band gap energy. The estimated band gaps were 3.31 eV, 3.13 eV, 2.7 eV and 2.89 eV for $N_{1-x}K_xVPF$ /C (x=0, 0.03, 0.08 and 0.13) samples, respectively. The change of band gap will affect the change of electronic conductivity of the material [30]. It is generally believed that the smaller the band gap energy of a material is, the easier it is for electrons to jump from the valence band to the conduction band, thus leading to that $N_{0.92}K_{0.08}VPF/C$ might be most suitable one for improving electronic conductivity. Furthermore, the electron conductivity was captured in the pressure range of 2-30 MPa. As shown in the Figure 3l, all electronic conductivities increased with the rising pressure. Under the 10 M pa, the electronic conductivities of $N_{1-x}K_xVPF/C$ (x=0.03, 0.08 and 0.13) samples were 2.62×10^{-5} S cm^{-1}, 3.78×10^{-5} S cm^{-1}, 3.18×10^{-5} S cm^{-1} at 25 °C, respectively, which

were higher than that of pristine NVPF/C (7.95×10^{-6} S cm^{-1}). Apparently, the change of electron conductivity was consistent with the change of band gap, revealing the highest electronic conductivity of $N_{0.92}K_{0.08}$VPF/C. Nitrogen adsorption-desorption measurement can be used to characterize the specific surface area and pore characteristics of materials. Figure S4 illustrated nitrogen adsorption-desorption isotherms and pore size distributions of $N_{1-x}K_x$VPF/C (x =0, 0.03, 0.08, and 0.13) samples. The BET surface areas of $N_{1-x}K_x$VPF/C (x = 0, 0.03, 0.08, and 0.13) samples were 7.0 $m^2 g^{-1}$, 8.1 $m^2 g^{-1}$, 12.9 $m^2 g^{-1}$, 9.2 $m^2 g^{-1}$, and the average pore sizes were 10.1 nm, 10.7 nm, 7.4 nm and 10.3 nm, respectively. As we can see, the $N_{0.92}K_{0.08}$VPF/C had the highest surface area and the lowest pore size, which could be helpful for the electrochemical reaction. Besides, in order to evaluate the wetting ability of the $NaClO_4$ electrolyte on the surface of the material, the contact angle between the $NaClO_4$ electrolyte and the samples was tested after the material was pressed. The results shown in Figure S5 illustrated the surface wet ability of a $NaClO_4$ electrolyte droplet on the NVPF/C and $N_{0.92}K_{0.08}$VPF/C. It was clear that $N_{0.92}K_{0.08}$VPF/C showed the smaller contact angle of 45.4° at the $NaClO_4$ and $N_{0.92}K_{0.08}$VPF/C interface compared with that at $NaClO_4$ and NVPF/C interface (65.2°). After 5s, the contact angle at the $NaClO_4$ and $N_{0.92}K_{0.08}$VPF/C interface dropped to 12.8°, while the contact angle between $NaClO_4$ and NVPF/C interface was still 16.4°, disclosing that the $N_{0.92}K_{0.08}$VPF/C had better contact with $NaClO_4$ electrolyte.

To investigate the electrochemical reaction kinetics of samples, cyclic voltammetry (CV) tests of samples in the potential window of 2.5-4.3 V vs. Na/Na^+ at a scan rate of 0.1 mV s^{-1} were carried out. As shown in Figure 4a,b and Figure S6, the CV profiles and dQ/dV plots of $N_{1-x}K_x$VPF/C (x=0, 0.03, 0.08 and 0.13) suggesting that the K^+ doped NVPF can effectively decrease the structure polarization in the charge/discharge and suppress the voltage hysteresis for high performance SIBs, and the $N_{0.92}K_{0.08}$VPF/C sample meaning the occurrence of the smallest polarization and a highly reversible phase transition during sodiation and (de)sodiation.

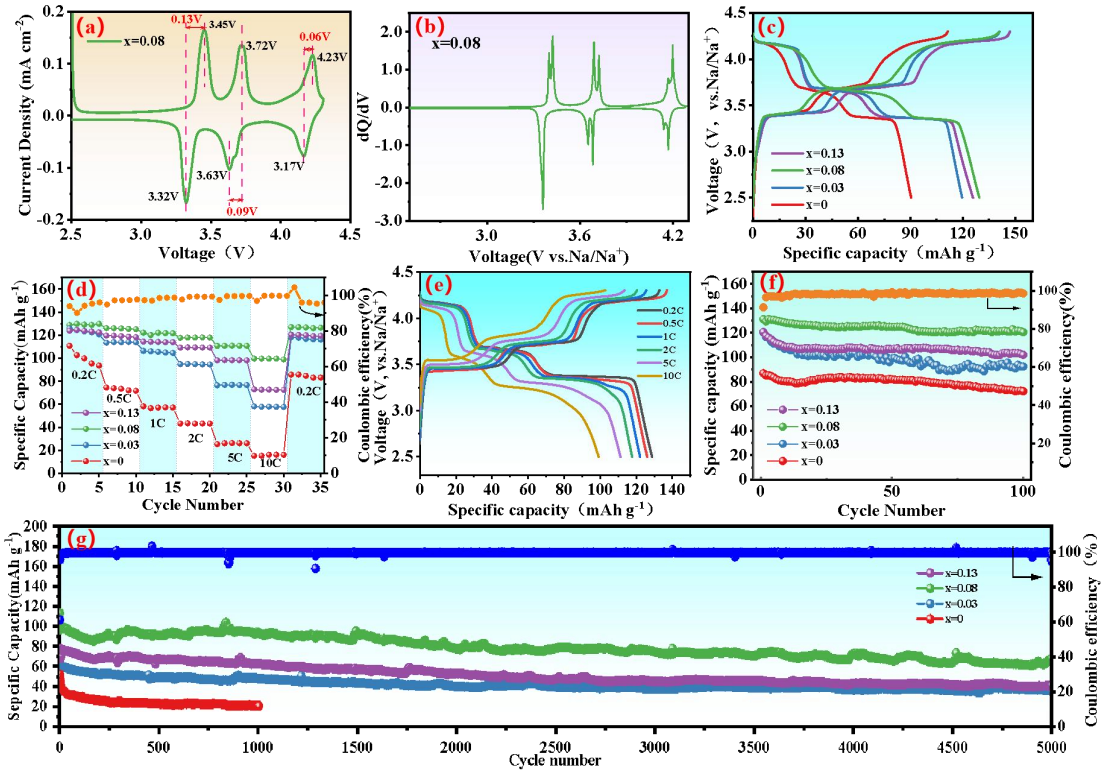

Figure 4 (a) Cyclic voltammetry curves of $N_{1.92}K_{0.08}VPF/C$ sample at a scan rate of 0.1 mV s^{-1}. (b) The dQ/dV curves for the first cycles of $N_{1.92}K_{0.08}VPF/C$ sample at 0.2 C. (c) Charge/discharge curves of $N_{1-x}K_xVPF/C$ (x=0, 0.03, 0.08 and 0.13) samples at a current density of 0.2 C within the voltage range of 2.5-4.3 V. (d) Rate capabilities of $N_{1-x}K_xVPF/C$ (x=0, 0.03, 0.08 and 0.13) samples. (e) Charge and discharge curves of $N_{0.92}K_{0.08}VPF/C$ electrode at various rates from 0.2 to 10 C. (f) Cycling performance of $N_{1-x}K_xVPF/C$ (x=0, 0.03, 0.08 and 0.13) samples at 0.2 C. (e) Cycling performance of $N_{1-x}K_xVPF/C$ (x=0, 0.03, 0.08 and 0.13) samples at 10 C.

The galvanostatic charge-discharge profiles for the first cycles of all the samples at 0.2 C under a potential window of 2.5-4.3 V were displayed in Figure 4c. Three pairs of potential plateaus at approximately 3.4 V, 3.7 V and 4.2 V could be observed obviously, corresponding to the redox pair of V^{3+}/V^{4+} with two Na^+ extraction/insertion reactions, in accordance with above CV results. Besides, the K^+ substituted samples exhibited higher specific capacity and better reversibility than pristine NVPF/C. With the increase of the doping amount of K^+, $N_{1-x}K_xVPF/C$ (x = 0,0.03, 0.08 and 0.13) samples could deliver the first discharge capacities of 90.4, 119.6, 128.8 and 125.8 mAh g^{-1} at 0.2 C, respectively, manifesting an increasing first

and subsequent decreasing trend. In other words, among the three K^+ doped NVPFs, $N_{0.92}K_{0.08}$VPF/C could deliver the highest discharge capacity value of 128.8 mAh g^{-1}. The initial coulombic efficiencies (ICE) of $N_{1-x}K_x$VPF/C (x = 0,0.03, 0.08 and 0.13) samples were 81.1%, 84.8%,91.6% and 85.6%, respectively. Rate capabilities of $N_{1-x}K_x$VPF/C (x = 0,0.03, 0.08 and 0.13) samples from 0.2 C to 10 C were evaluated. According to Figure 4d, the discharge capacity of each sample decreased with the increase of current density. Specifically, the discharge capacity $N_{0.92}K_{0.08}$VPF/C at various current densities were up to 128.8, 126.1, 122.1, 117.1, 110.6, and 99.6 mAh g^{-1} at 0.2 C, 0.5 C, 1 C, 2 C, 5 C, and 10 C, respectively, which are all higher than the corresponding values of NVPF/C (110.8, 74.5, 58.2, 43.2, 25.4, and 15.2 mAh g^{-1}), $N_{0.97}K_{0.03}$VPF/C (125.9, 113.5, 106.3, 94.8, 76.5, and 58.1 mAh g^{-1}) and $N_{0.87}K_{0.13}$VPF/C (123.8, 119.6, 114.4, 109.2, 98.2, and 72.9 mAh g^{-1}). Especially, at a high rate of 10 C, the $N_{0.92}K_{0.08}$VPF/C could still deliver a specific capacity of 99.6 mAh g^{-1}. Compared with the capacity at 0.2 C, the capacity retention rate is 76.7% at 10 C, suggesting that even if the charge-discharge rate is increased by 50 times from 0.2 C to 10 C, the capacity is only 24.3% attenuated, lower than those of NVPF/C (86.2%), $N_{0.97}K_{0.03}$VPF/C (52.6%) and $N_{0.87}K_{0.13}$VPF/C (41.1%). In Figure 4e, the charge and discharge curves of $N_{0.92}K_{0.08}$VPF/C at different rates were shown, indicating that even at high rate of 10 C, an obvious discharge plateau of $N_{0.92}K_{0.08}$VPF/C could still be observed. Additionally, in Figure S7, the charge/discharge curves of $N_{0.92}K_{0.08}$VPF/C sample for 5th, 10th, 20th, 50th, 75th and 100th cycle at 0.2 C were displayed, illustrating that $N_{0.92}K_{0.08}$VPF/C could remain the charge/discharge curves without apparent change. It is noted that proper amount of K doping improves the structural stability and conductivity of the material, and ensures rapid sodium embedding/release in the process of high-rate cycle. Figure 4f exhibited the cyclic capacity of $N_{1-x}K_x$VPF/C (x =0, 0.03, 0.08 and 0.13) samples and the coulombic efficiency profiles of $N_{0.92}K_{0.08}$VPF/C at 0.2 C. It can be seen that the $N_{0.92}K_{0.08}$VPF/C displayed higher capacity and cycle stability than the other three samples at 0.2 C, together with a high coulombic efficiency of 92% after 100 cycles. Apart from that, the long-term cycling stabilities of sodium storage of $N_{1-x}K_x$VPF/C

(x = 0, 0.03, 0.08 and 0.13) at a high current density of 10 C were also revealed in Figure 4g. Apparently, the $N_{0.92}K_{0.08}VPF/C$ delivered an initial capacity of 113.3 mAh g^{-1}, and retained up to 82.5% of its capacity after 1000 cycles, higher than those of other samples (Table S2, Supporting Information). Even after ultralong lifespan of 5000 cycles, it could still exhibit a discharge capacity as high as 68.2 mAh g^{-1} and maintain capacity retention of 60.2%, demonstrating excellent cycling performance. Moreover, the corresponding charge/discharge curves of $N_{1-x}K_xVPF/C$ (x=0, 0.03, 0.08 and 0.13) at a current density of 10 C within the voltage range of 2.5-4.3 V were presented in Figure S8, illustrating a high capacity and obvious discharge plateau in $N_{0.92}K_{0.08}VPF/C$, matching with cycling test. Meanwhile, compared with other polyanion-type cathodes in recent works as shown in Table S3, the $N_{0.92}K_{0.08}VPF/C$ could offer a superior cycling property and higher capacity retention. Indeed, the $Na_3V_2(PO_4)_2F_3$ via in situ substitution K^+ doped could be an appealing material for sodium-ion batteries with suppressed voltage hysteresis and ultralong cycle lifespan. In conclusion, regarding suppressing voltage hysteresis and increasing cycle life, the optimal K^+ cation doping was found in $N_{0.92}K_{0.08}VPF/C$.

To further clarify the influence of K^+ doping on the electrochemical performance, the kinetic properties of $N_{1-x}K_xVPF/C$ (x=0,0.03, 0.08 and 0.13) samples were

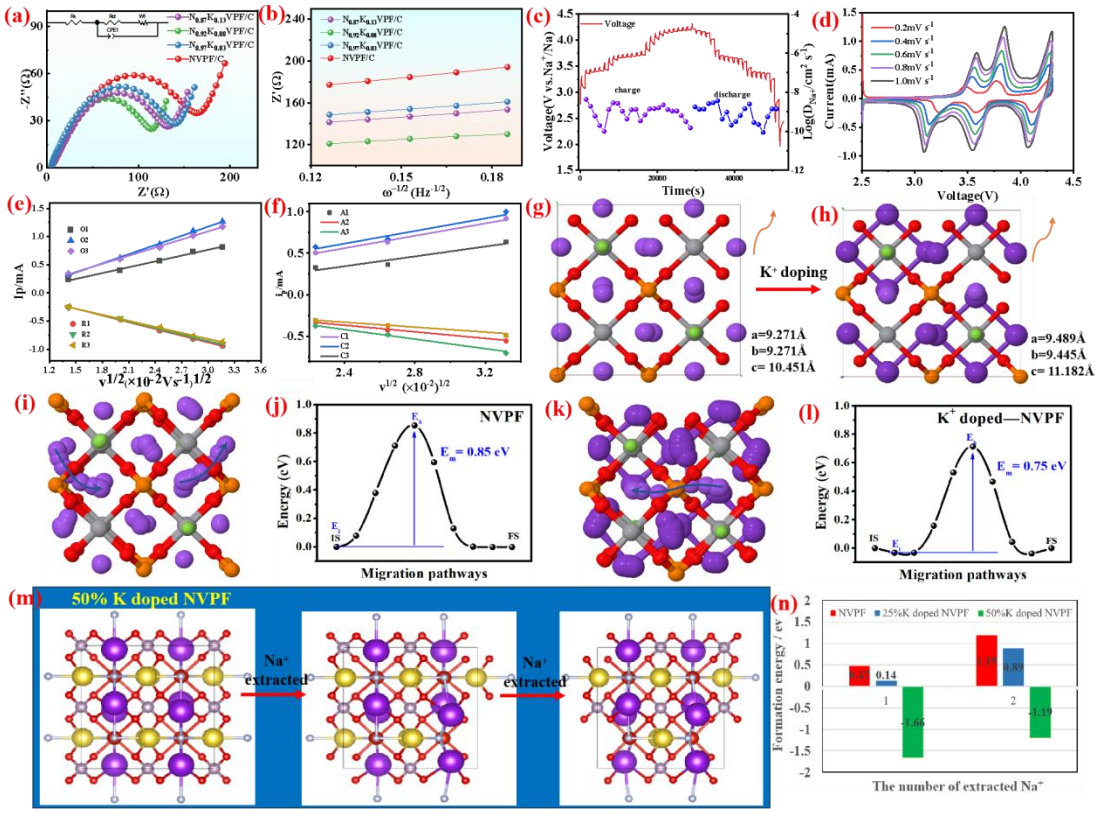

Figure 5 (a) Nyquist plots of fresh $N_{1-x}K_xVPF/C$ (x=0,0.03,0.08 and 0.13) samples (The equivalent circuit is inset graph used for fitting the experimental data). (b) Fitting Z' and $\omega^{-1/2}$ of fresh $N_{1-x}K_xVPF/C$ (x=0,0.03,0.08 and 0.13) samples. (c) GITT electrochemical charge/discharge curves of $N_{0.92}K_{0.08}VPF/C$. (d) CV curves of the $N_{0.92}K_{0.08}VPF/C$ sample at various scan rates. (e-f) corresponding relationship of $v^{1/2}$ and I_p for $N_{0.92}K_{0.08}VPF/C$ and NVPF/C. (g-h) NVPF crystal changes before and after K doping. (i-j) Scheme presenting the Na^+ migration in NVPF and corresponding migration energy barrier. (k-l) Scheme presenting the Na^+ migration in K^+ doped NVPF and corresponding migration energy barrier. (m) Crystal structure change of 50% K doped NVPF derived from the extraction of 1 and 2 Na ions. (n) The formation energies of NVPF, 25% K doped NVPF and 50% K doped NVPF after 1 and 2 Na^+ extracted from the structures.

investigated by using EIS (Figure 5a, the inset illustration is the equivalent circuit diagram). A semicircle in the high-frequency region and a straight line in the low-frequency region can be obviously observed from the Nyquist plots of all $N_{1-x}K_xVPF/C$ (x=0,0.03, 0.08 and 0.13) samples. The value of the semicircle diameter on the Z' axis can be approximated as the charge transfer resistance (R_{ct}), attributed to the Na^+ migration through the interface between the particle surface layer and the

electrolyte [36]. The curves of Z' and $\omega^{-1/2}$ and the fitted slope lines in the Warburg region from EIS spectra were presented in Figure 5b. Parameters calculated from the curves were listed in Table S4. Clearly, the R_{ct} values of $N_{1-x}K_xVPF/C$ (x=0, 0.03, 0.08 and 0.13) samples were 183.3, 145.3, 122.4 and 140.2 Ω, respectively, in consistence with the trend of electronic conductivity. Based on the equations, sodium ion diffusion coefficient is only related with Warburg factor σ, i.e., the lower Warburg factor σ, the higher sodium ion diffusion coefficient. By comparison, the K-doped samples possessed a higher Na^+ diffusion coefficient than pure NVPF/C, which proves that K doping can increase the diffusion of sodium ions and improve the electrochemical performance. Note that $N_{0.92}K_{0.08}VPF/C$ sample had the highest Na^+ diffusion coefficient and interestingly the variation trend of the Na^+ diffusion coefficient is similar to the reported work previously [10], [24]. In addition, the constant current intermittent titration (GITT) test was carried out under the conditions of voltage range of 2.5-4.3 V and constant current density of 0.5 C to calculate the sodium ion diffusion coefficient of NVPF/C and $N_{0.92}K_{0.08}VPF/C$ (Figure 5c and Figure S9). The diffusion coefficient is calculated by the following formula: $D_{Na^+}=\frac{4}{\tau\pi}\left(\frac{m_B V_M}{M_B S}\right)^2\left(\frac{\Delta E_s}{\Delta E_\tau}\right)^2$. The calculated sodium ion diffusion coefficient value of $N_{0.92}K_{0.08}VPF/C$ was in the range of 2.59×10^{-10}~6.98×10^{-9} cm^2 s^{-1} and the average value was 2.20×10^{-9} cm^2 s^{-1}, higher than those of NVPF/C (the range of 8.77×10^{-11}~4.29×10^{-9} cm^2 s^{-1} and the average value 1.26×10^{-9} cm^2 s^{-1}). And it can be found that the fluctuation of D_{Na+} in $N_{0.92}K_{0.08}VPF/C$ is smaller than that of NVPF/C, meaning the excellent Na^+ migration kinetics of $N_{0.92}K_{0.08}VPF/C$[37]. In order to further test the diffusion kinetics of Na^+, CV tests were carried out at different scanning rates. As shown in Figure 5d, with the increase of scanning rate, the cathode peak and anode peak moved to lower potential and higher potential, respectively, and the peak intensity and area were increased. The sodium ion diffusion coefficient D_{Na+} can be calculated by the Randles-Sevcik equation: $i_p=2.69\times10^5 n^{\frac{3}{2}} A D^{\frac{1}{2}} v^{\frac{1}{2}} c_0$. In this equation, I_p is the peak current, n the number of electrons transferred by the redox couple in the semi-reaction, A the electrode area, D the diffusion coefficient of Na^+, c

the intrinsic concentration of Na^+ (c=0.001 mol cm^{-3}), and n the potential scanning rate. It can be seen from Figure 5e that the peak current (I_p) was directly proportional to the square root ($v^{1/2}$) of the scanning rate, indicating that the sodiation/desodiation reactions was controlled by the ion diffusion mechanism.[25, 38] The D_{Na+} calculated by the formula was 3.67×10^{-10}~2.18×10^{-9} cm^2 s^{-1}, being consistent with the results obtained by GITT, which substantiates good reversibility and fast Na^+ diffusion kinetics in $N_{0.92}K_{0.08}$VPF/C. As comparison, in Figure S10, CV curves of the NVPF/C sample at various scan rates were also revealed. Moreover, as for NVPF/C, Figure 5e displayed the peak current (I_p) proportional to the square root ($v^{1/2}$) of the scanning rate, from which the calculated D_{Na+} was in the range of 2.41×10^{-10}~1.10×10^{-9} cm^2 s^{-1}, lower than that of $N_{0.92}K_{0.08}$VPF/C. More importantly, Na^+ migration energy barriers of NVPF before and after K^+ doping was calculated by DFT. The corresponding crystal structures were shown in Figure 5g-h. After K^+ doping, the cell parameters a, b and c all became larger, revealing that K^+ doping broadens the migration channel of Na^+ and is more conducive to the migration of Na^+. In Figure 5i-j, the scheme presenting the Na^+ migration in NVPF and the corresponding migration energy barrier were manifested, respectively. As comparison, Figure 5k-l indicated the scheme presenting the Na^+ migration in K^+ doped NVPF and corresponding migration energy barrier. As we can see, thanks to K^+ doping, the migration energy barrier (E_m) of Na^+ in K^+ doped NVPF was reduced from 0.85 eV to 0.75 eV, clearly suggesting that K^+-doped NVPF was more favorable for the migration of Na^+. In addition, to simulate energy of the de-sodiation in K doped NVPF with different doping amounts, DFT was carried out to obtain the formation energies after the extraction of a certain of Na (1 and 2 Nas) on NVPF with different K contents. The NVPF, 25% K doped NVPF and 50% K doped NVPF crystals were conducted as model structures. Figure 5m and Figure S11 revealed the crystal structure changes of NVPF, 25% K doped NVPF and 50% K doped NVPF, respectively, which were derived from the extraction of one and two sodium ions. Meanwhile, in Table S5, the formation energy of NVPF- Na_x and KNVPF-Na_x and the total energy of NVPF-Na_x, KNVPF- Na_x, NVPF, KNVPF and Na atoms were listed. As shown in Figure 5n, it was found that the calculated

formation energies of NVPF, 25% K doped NVPF and 50% K doped NVPF after one sodium ion extracted from the structures were 0.47 eV, 0.14 eV and -1.66 eV, respectively, suggesting that the 50% K doped NVPF structure was the most favorable for first Na^+ extraction. Likewise, the calculated formation energies of NVPF, 25% K doped NVPF and 50% K doped NVPF after two sodium ions extracted from the structures were 1.19 eV, 0.89 eV and -1.19 eV, respectively, meaning that the second Na^+ could be extracted the most easily from 50% K doped NVPF. Apparently, it could be gotten that the more amount of K^+ cation doping, the lower formation energies after the extraction of a certain of Na (1 and 2 Nas) on K doped NVPF, which appears that the $N_{0.87}K_{0.13}$VPF/C sample with highest K^+ doping rather than $N_{0.92}K_{0.08}$VPF/C is supposed to display the most excellent battery performances, obviously disagreeing with the as-obtained results. It is to be observed that a crucial parameter of the crystalline structural change induced by sodiation and (de)sodiation was not considered in the simulation. Also, it is assumed that a high K^+ doping can surely lead to the enlarged crystal structure, being favorable for sodium ion migration. So, in theory there should be an appropriate doping amount of K^+ to replace Na^+ sites in K-doped NVPF, which not only leads to rapid sodium ion migration but also ensures a highly reversible phase transition. In order to verify this assumption, the sample of KVPF, in which Na cations of NVPF were fully substituted by K^+, was prepared for comparison. Figure S12 displayed the SEM image, XRD pattern and EDS analysis of KVPF with K cation fully substituted Na. It was seen that the KVPF particles with irregular sizes and shapes were obtained. Moreover, all diffraction peaks of KVPF matched with NVPF crystalline structure and K, P, F and V elements were present from EDS analysis, proving the successful synthesis of KVPF. In Figure S13, from electrochemical test, a capacity of 13.9 mAh g^{-1} for KVPF was obtained after 26 cycles at 0.2 C, showing a very poor cycling performance. Clearly, it was indicated that the full K cation substituting Na was not in favor for sodium storage performance, confirming the above assumption. To obtain high performance sodium ion batteries, the rapid Na^+ diffusion and stable phase transition should be realized by finding the optimal doping concentration. Therefore, to suppress voltage hysteresis and improve

cycling lifespan, the optimal K^+ doping amount in $N_{0.92}K_{0.08}VPF/C$ was found.

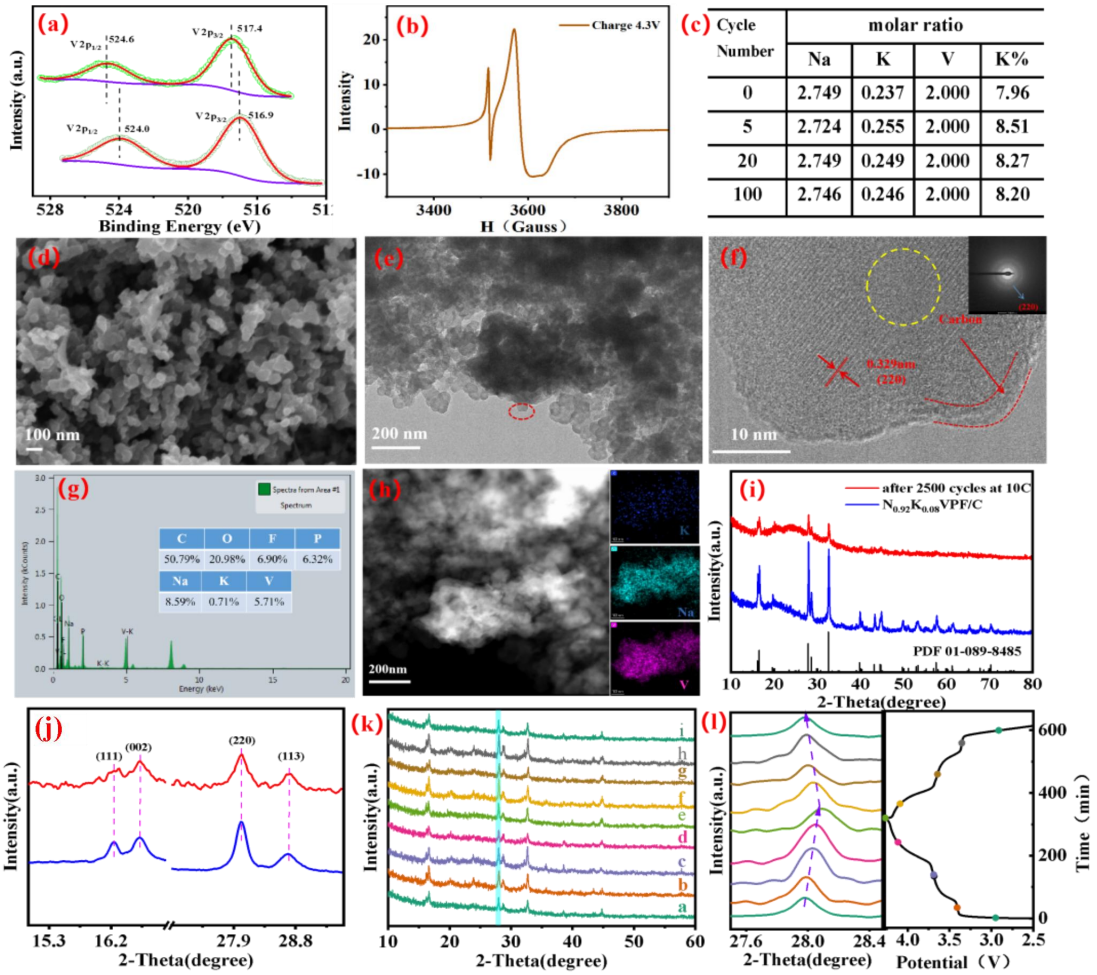

Cycle Number	molar ratio			
	Na	K	V	K%
0	2.749	0.237	2.000	7.96
5	2.724	0.255	2.000	8.51
20	2.749	0.249	2.000	8.27
100	2.746	0.246	2.000	8.20

Figure 6 (a) XPS V 2p fine spectra of $N_{0.92}K_{0.08}VPF/C$ sample before (lower curve) and after (upper curve) being charged to 4.3 V at 2 C. (b) EPR spectrum of $N_{0.92}K_{0.08}VPF/C$ charged to 4.3 V. (c) ICP-MS data of $N_{0.92}K_{0.08}VPF/C$ sample after different number of cycles at 10 C. (d) SEM of $N_{0.92}K_{0.08}VPF/C$ after 2500 cycles at 10 C. (e-f) TEM images and SAED pattern of $N_{0.92}K_{0.08}VPF/C$ after 2500 cycles at 10 C. (g) EDS spectrum of $N_{0.92}K_{0.08}VPF/C$ after 2500 cycles at 10 C. (h) TEM elemental mappings of Na, K and V. (i) XRD of $N_{0.92}K_{0.08}VPF/C$ before and after 2500 cycles at 10 C. (j) The enlarged diffraction peaks at selected acquisition angle between 15° to 29°. (k) Ex-situ XRD patterns of $N_{0.92}K_{0.08}VPF/C$ electrode charged and discharged at different voltages under 0.5 C. (l) The enlarged diffraction peaks at selected acquisition angle between 27.6° and 28.4°.

To further have in-depth understanding of the structural change of K^+-doped NVPF after cycling, the most promising sample of $N_{0.92}K_{0.08}VPF/C$ was obtained by disassembling the coin battery after cycling for phase and morphology

characterization. Figure S14 manifested the XPS result of $N_{0.92}K_{0.08}VPF/C$ after charging to 4.3 V at a current density of 2 C. Figure S14a displayed the full spectrum of XPS. The peaks of all elements of Na, K, V, P, F and C appeared, indicating that the elemental composition of the substance remained unchanged before and after charging. Specifically, in Figure S14b, the fine spectrum of C 1s could be deconvolved into three Gaussian peaks, corresponding to C-C (284.6 eV), C-O (285.7 eV) and C=O (286.5 eV), respectively. Figure S14c indicated the fine spectrum of K 2p. It could be seen that after charging to 4.3 V, both peaks of K 2p were obviously shifted to the higher binding energy. Besides, XPS V 2p fine spectra of $N_{0.92}K_{0.08}VPF/C$ sample before (lower curve) and after (upper curve) being charged to 4.3 V at 2 C were displayed in Figure 6a. It was found that V 2p of $N_{0.92}K_{0.08}VPF/C$ sample after charging showed higher binding energy, which could be attributed to the appearance of V^{4+}, signifying the existence of a mixture of V^{3+} and V^{4+} in charged state of $N_{0.92}K_{0.08}VPF/C$ because of Na^+ extraction. On the other hand, EPR measurement was carried out to study the disorder or defects of the charged $N_{0.92}K_{0.08}VPF/C$ [39]. As exhibited in Figure 6b, compared to the original $N_{0.92}K_{0.08}VPF/C$, $N_{0.92}K_{0.08}VPF/C$ after being charged to 4.3 V could deliver a narrow peak of g=2.0, which can be attributed to oxygen vacancy [40-41]. Moreover, the peak at 3598 Gauss became broader, which can be attributed to the presence of V^{4+}, matching with XPS analysis [32]. In general, the doped cations tend to occupy positions where the substituted ions and dopants have similar electronegativity and ionic radii. Li et al. [42] proposed a mathematical equation to predict the occupation positions of doping atoms in polyanionic materials. By comparing the deviation calculated from the electronegativity and radius between the dopant ion and the dopant ion, the preferred doping position can be determined from the smaller deviation. For $Na_3V_2(PO_4)_2F_3$, the deviation (D_{Na}) of doping K^+ at the Na^+ site can be expressed as follows:

$$D_{Na}=|(\chi_K-\chi_{Na})/\chi_{Na}|+|(r_K-r_{Na})/r_{Na}|$$

where χ_K and r_K are electronegativity and radius of the K^+, and χ_{Na} and r_{Na} are electronegativity and radius of the Na^+. The values of D_{Na} and D_V were 0.674 and 1.296, respectively, indicating that K^+ might replace Na^+ because of the smaller

deviation of K^+. As we know, there are two different Na sites in NVPF and the occupancy rate is 2:1. Meanwhile, the completely occupied site is Na(1), and the other partially occupied site is Na(2). In the process of charge-discharge reaction, Na^+ at Na(1) site does not participate in embedding/ release [43]. As a result, it was assumed that the doped K^+ ion probably occupied the Na(1) position or Na(2) position. Figure 6c displayed ICP-MS data of $N_{0.92}K_{0.08}$VPF/C sample after different number of cycles (5, 20 and 100 times) at 10 C. Apparently, the content of K^+ ions in $N_{0.92}K_{0.08}$VPF/C remained unchanged (i.e., 8.57%, 8.27% and 8.20% after 5, 20 and 100 cycles, respectively). At the same time, EDS elemental mappings of Na, V and K of $N_{0.92}K_{0.08}$VPF/C at 10 C after 5, 20 and 100 cycles were presented in Figure S15, illustrating that obvious existence and uniform distribution of K^+ ions after cycling. The above results clearly manifested that doped K^+ did not participate in the sodium embedding/extraction during the charge-discharge process. Consequently, the doping position of K^+ ion is located at the Na1 site via in situ substitution, and it plays the role of pillar in the whole process to improve the long-term cycling ability and stability of the K-doped NVPF. In order to verify the optimal K concentration replacement pillar effect, $N_{0.92}K_{0.08}$VPF/C cycled 2500 times at a current density of 10 C was characterized. The morphology and size of the $N_{0.92}K_{0.08}$VPF/C after 2500 cycles at 10 C were examined by SEM (Figure 6d and Figure S16) and TEM (Figure 6e-f), displaying that the particles were pulverized to some extent and that their sizes were reduced from ~200nm to ~100nm compared with these of original $N_{0.92}K_{0.08}$VPF/C. The pulverization of $N_{0.92}K_{0.08}$VPF/C particles could be attributed to the distortions caused by the higher utilization of ion during the cycle [44]. On the other hand, although the particles were pulverized, almost all of the particles were not significantly fractured, which reflects the benefit of K^+ as a doping ion and carbon coating (preventing NVPF from being corroded by the electrolyte) in stabilizing the structure of NVPF materials [41, 45-46]. Figure 6f (captured from the red square area in Figure 6e) illustrated the HRTEM image of $N_{0.92}K_{0.08}$VPF/C after 2500 cycles at 10 C. The crystallinity of the $N_{0.92}K_{0.08}$VPF/C decreased slightly (shown in the yellow square area) and the d spacing of (200) plane increased from 0.453 nm to 0.457nm.

Meanwhile, the carbon layer became uneven and fractured, and the selected area electron diffraction (SAED) pattern demonstrated obvious spot for crystal of (200) plane matching with HRTEM. EDS spectrum in Figure 6g displayed the atomic ratio of elements of $N_{0.92}K_{0.08}$VPF/C after 2500 cycles at 10 C. After calculation, the content of K was 8.29%, which was almost unchanged compared with that before cycling. These results further proved that the doping position of K^+ should be Na(1) and play a supporting role. As seen in TEM elemental mappings of $N_{0.92}K_{0.08}$VPF/C after 2500 cycles at 10 C (in Figure 6h), all the Na, K and V elements were uniformly distributed in the materials, proving the high structural stability of K^+ doped NVPF. The circulating active material was collected and XRD was shown in Figure 6i. The enlarged diffraction peaks at selected acquisition angle between 15° to 29° were exhibited in Figure 6j. Surprisingly, the XRD pattern of the $N_{0.92}K_{0.08}$VPF/C after 2500 cycles could be indexed to the standard JCPDS card of NVPF (PDF No.01-089-8488), suggesting no observed phase change. In addition, to further investigate the structural stability of the $N_{0.92}K_{0.08}$VPF/C sample during cycles, ex-situ XRD tests were conducted at different voltage levels (selected by cyclic voltammetry curve in Figure 6c for the 1st cycle at 0.5 C. As displayed in Figure 6k, the diffraction peaks of $N_{0.92}K_{0.08}$VPF/C at different voltage in the charge and discharge were well-matched with the standard JCPDS card (PDF No.01-089-8488), which indicated the NVPF crystal phase without obvious change. As presented in the Figure 6l, we can see the enlarged diffraction peaks of (220) crystal face between 27.6° and 28.4° in the pattern of XRD. The peak of the plane of (220) at 27.9° was seen at initial voltage and finally moved to 28.0° after being charged to 4.3V with three different voltage platforms of 3.45 V, 3.72 V and 4.23 V, which could be ascribed to the enlarged variations of the lattice parameters after the extraction of Na^+. After the discharge of three voltage platforms of 4.17 V, 3.63 V and 3.32 V to 2.5 V, the peak value returned back to 27.9°, which suggesting the reversible phase transition of crystal structure, verifying the superior structural stability of $N_{0.92}K_{0.08}$VPF/C sample during charging and discharging. Figure S17 displayed the EDS elemental mappings of Na, V and K of $N_{0.92}K_{0.08}$VPF/C sample at 0.5 C after being charged to 3.45 V, 3.74 V, 4.24 V and

4.3 V and discharged to 2.5 V, indicating that K^+ did not break away from the crystal structure and played a pillar role in the charging and discharging process. These results approved that the doping site of K^+ was Na (1), meaning that the K^+ cation plays a pillar role in NVPF structure to improve ionic conductivity and improve the structural stability of materials.

3. Conclusions

In summary, K^+ was introduced into the Na site of NVPF/C by sol-gel method to improve the electronic conductivity and ionic conductivity. Moreover, the changes of electronic conductivity and ionic conductivity revealed a trend of first increasing and subsequent decreasing, which is similar to the change trend of transition metal replacing V site. The doping of K reduced the energy of the band gap energy (E_g), which is beneficial to the optimization of intrinsic electron conductivity. The doped K^+ occupies the Na1 position and plays a key role in the process of charging and discharging, ensuring a high Na^+ mobility. Based on the advantages brought by K doping, $N_{0.92}K_{0.08}$VPF/C sample had the best conductivity and structural stability, thus providing the best electrochemical performance. As the cathode of sodium ion battery, the specific capacity of 0.2 C was as high as 128.8 mA h g^{-1}, and the rate performance of 10 C was excellent, the value of which was up to 113.3 mA h g^{-1}. After 100 cycles at a low rate of 0.2 C, with a high retention of 92%, and after ultralong cycle lifespan of 5000 cycles at a rate of 10 C, the retention rate was 60.2%.

Funding

This work was supported by the National Natural Science Foundation of China (No. 22075227) and China Postdoctoral Science Foundation (No. 2021M692605).

Conflict of Interest

There is no conflict to declare.

Data Availability statement

The data are available from the corresponding author on reasonable request.

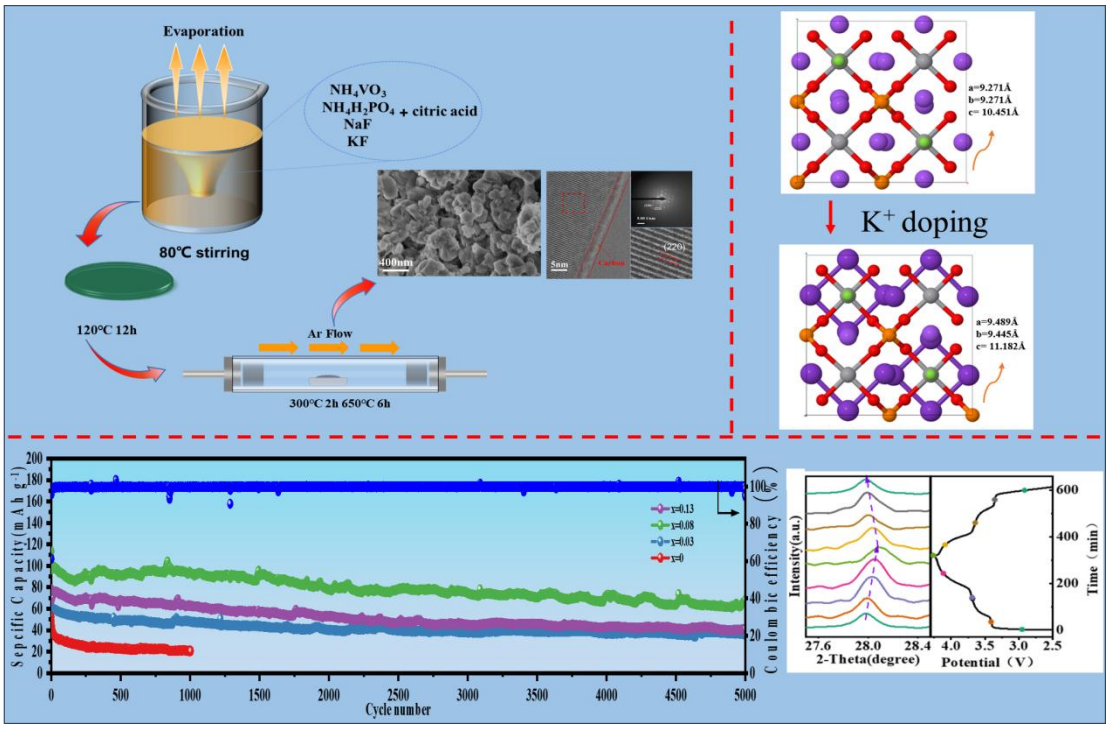

Thanks to the rapid Na^+ migration and reversible phase transition of K^+ doping in $Na_3V_2(PO_4)_2F_3$ cathode material, the as-obtained modified composite delivered significantly enhanced performance of sodium ion batteries.

References

[1] X. Xiang, K. Zhang, J. Chen, *Adv. Mater.* **2015**, *27*, 5343-5364.

[2] V. Palomares, P. Serras, I. Villaluenga, K. B. Hueso, J. Carretero-González, T. Rojo, *Energy Environ. Sci.* **2012**, *5*.

[3] B. Lee, E. Paek, D. Mitlin, S. W. Lee, *Chem. Rev.* **2019**, *119*, 5416-5460.

[4] S.-H. Zhuang, C.-C. Yang, M. Zheng, S. Rengapillai, S. Marimuthu, Y.-S. Chiang, B. K. Chang, C.-H. Huang, W.-R. Liu, *Surf. Coat. Tech.* **2022**, *434*, 128184.

[5] L. Zhao, X. Rong, Y. Niu, R. Xu, T. Zhang, T. Li, Y. Yu, Y. Hou, *Small* **2020**, *16*.

[6] J. Barker, R. K. B. Gover, P. Burns, A. J. Bryan, *Electrochem. Solid-State Lett.* **2006**, *9*, A190.

[7] T. Jiang, G. Chen, A. Li, C. Wang, Y. Wei, *J. Alloy. Compd.* **2009**, *478*, 604-607.

[8] M. Bianchini, N. Brisset, F. Fauth, F. Weill, E. Elkaim, E. Suard, C. Masquelier, L. Croguennec, *Chem. Mater.* **2014**, *26*, 4238-4247.

[9] Q. Liu, D. Wang, X. Yang, N. Chen, C. Wang, X. Bie, Y. Wei, G. Chen, F. Du, *J. Mater. Chem. A* **2015**, *3*, 21478-21485.

[10] W. Liu, H. Yi, Q. Zheng, X. Li, H. Zhang, *J. Mater. Chem. A* **2017**, *5*, 10928-10935.

[11] D. A. Puspitasari, J. Patra, I. M. Hung, D. Bresser, T. C. Lee, J. K. Chang, *ACS Sustain. Chem. Eng.* **2021**, *9*, 6962-6971.

[12] A. Criado, P. Lavela, C. Perez-Vicente, G. F. Ortiz, J. L. Tirado, *J. Electroanal. Chem.* **2020**, *856*.

[13] Y. Zhang, S. Guo, H. Xu, *J. Mater. Chem. A* **2018**, *6*, 4525-4534.

[14] H. Yi, M. Ling, W. Xu, X. Li, Q. Zheng, H. Zhang, *Nano Energy* **2018**, *47*, 340-352.

[15] L. Li, Y. Xu, R. Chang, C. Wang, S. He, X. Ding, *Energy Storage Mater.* **2021**, *37*, 325-335.

[16] Y. U. Park, D. H. Seo, H. Kim, J. Kim, S. Lee, B. Kim, K. Kang, *Adv. Funct. Mater.* **2014**, *24*, 4603-4614.

[17] W. Song, X. Ji, Z. Wu, Y. Yang, Z. Zhou, F. Li, Q. Chen, C. E. Banks, *J. Power Sources* **2014**, *256*, 258-263.

[18] M. Bianchini, N. Brisset, F. Fauth, F. Weill, E. Elkaim, E. Suard, C. Masquelier, L. Croguennec, *Chem. Mater.* **2014**, *26*, 4238-4247.

[19] X. Dong, Y. L. Xu, L. L. Xiong, X. F. Sun, Z. W. Zhang, *J. Power Sources* **2013**, *243*, 78-87.

[20] H. Yi, L. Lin, M. Ling, Z. Lv, R. Li, Q. Fu, H. Zhang, Q. Zheng, X. Li, *ACS Energy Lett.* **2019**, *4*, 1565-1571.

[21] A. Mukherjee, T. Sharabani, R. Sharma, S. Okashy, M. Noked, *Batteries & Supercaps* **2020**, *3*, 510-518.

[22] Y. Qi, L. Mu, J. Zhao, Y. S. Hu, H. Liu, S. Dai, *Angew. Chem., Int. Ed.* **2015**, *54*, 9911-9916.

[23] J. F. Ou, J. Q. Wang, S. Liu, B. Mu, J. F. Ren, H. G. Wang, S. R. Yang, *Langmuir* **2010**, *26*, 15830-15836.

[24] M. X. Wang, K. Wang, X. B. Huang, T. Zhou, H. S. Xie, Y. R. Ren, *Ceram. Int.* **2020**, *46*, 28490-28498.

[25] L. N. Bi, Z. Miao, X. Y. Li, Z. C. Song, Q. J. Zheng, D. M. Lin, *Electrochim. Acta* **2020**, *337*.

[26] F. Tuinstra, J. L. Koenig, *J. Chem. Phys.* **1970**, *53*, 1126-1130.

[27] W. Yang, W. He, X. Zhang, G. Yang, J. Ma, Y. Wang, C. Wang, *Chem. Electro. Chem.* **2019**, *6*, 2020-2028.

[28] D. Yang, et al., *Carbon* **2009**, *47*, 145-152.

[29] W. Zheng, R. Gao, T. Zhou, X. Huang, *Solid State Ionics* **2018**, *324*, 183-190.

[30] Z.-Y. Gu, J.-Z. Guo, Z.-H. Sun, X.-X. Zhao, W.-H. Li, X. Yang, H.-J. Liang, C.-D. Zhao, X.-L. Wu, *Science Bulletin* **2020**, *65*, 702-710.

[31] L. Deng, F.-D. Yu, Y. Xia, Y.-S. Jiang, X.-L. Sui, L. Zhao, X.-H. Meng, L.-F. Que, Z.-B. Wang, *Nano Energy* **2021**, *82*, 105659.

[32] P. Serras, V. Palomares, A. Goñi, I. Gil de Muro, P. Kubiak, L. Lezama, T. Rojo, *J. Mater. Chem.* **2012**, *22*.

[33] J. M. Le Meins, M. P. Crosnier-Lopez, A. Hemon-Ribaud, G. Courbion, *J.Solid State Chem.* **1999**, *148*, 260-277.

[34] M. A. Butler, D. S. Ginley, M. Eibschutz, *J. Appl. Phys.* **1977**, *48*, 3070-3072.

[35] C. Xu, W. Xiao, T. Liu, F. Sun, J. Zheng, S. Peng, X. Liu, F. Pan, W. Yang, H.-k. Mao, *J. Mater. Chem. A* **2017**, *5*, 19390-19397.

[36] K. Liang, S. Wang, H. Zhao, X. Huang, Y. Ren, Z. He, J. Mao, J. Zheng, *Chem. Eng. J.* **2022**, *428*, 131780.

[37] X. Fan, Y. Zhu, C. Luo, L. Suo, Y. Lin, T. Gao, K. Xu, C. Wang, *ACS Nano* **2016**, *10*, 5567-5577.

[38] Y. Cai, X. Cao, Z. Luo, G. Fang, F. Liu, J. Zhou, A. Pan, S. Liang, *Adv. Sci.* **2018**, *5*.

[39] G. Chen, Q. Huang, T. Wu, L. Lu, *Adv. Funct. Mater.* **2020**, *30*, 2001289.

[40] B. Hu, et al., *J. Power Sources* **2021**, *516*.

[41] J. Li, J. Cheng, Y. Chen, C. Wang, L. Guo, *Ionics* **2021**, *27*, 181-190.

[42] K. Y. Li, J. J. Shao, D. F. Xue, *Funct. Mater. Lett.* **2013**, *6*.

[43] W. Song, X. Cao, Z. Wu, J. Chen, Y. Zhu, H. Hou, Q. Lan, X. Ji, *Langmuir* **2014**, *30*, 12438-12446.

[44] W. Li, H. Y. Asl, Q. Xie, A. Manthiram, *J. Am. Chem. Soc.* **2019**, *141*, 5097-5101.

[45] Q. Wang, M. Zhang, C. Zhou, Y. Chen, *J Phys. Chem. C* **2018**, *122*, 16649-16654.

[46] N.-B. Jiang, L.-L. Zhang, C.-X. Cui, L. Gao, X.-L. Yang, *ACS Appl. Energ. Mater.* **2022**, *5*, 249-256.